Chapter 9

Basics of Chemical Exchange Saturation Transfer (CEST) Magnetic Resonance Imaging

Kenya Murase

Additional information is available at the end of the chapter

http://dx.doi.org/10.5772/intechopen.71645

Abstract

Chemical exchange saturation transfer (CEST) is one of the contrast mechanisms in magnetic resonance imaging (MRI) and has been used to detect dilute proteins through the interaction between bulk water and labile solute protons. Amide proton transfer (APT) MRI has been developed for imaging diseases such as acute stroke. Moreover, various CEST agents have been explored to enhance the CEST effect. The contrast mechanism of CEST or APT MRI, however, is complex and depends not only on the concentration of amide protons or CEST agents and exchange properties, but also varies with imaging parameters such as radiofrequency (RF) power and magnetic field strength. When there are multiple exchangeable pools within a single CEST system, the contrast mechanism of CEST becomes even more complex. Numerical simulations are useful and effective for analyzing the complex contrast mechanism of CEST and for investigating the optimal imaging parameter values. In this chapter, we present the basics of CEST or APT MRI and a simple and fast numerical method for solving the time-dependent Bloch-McConnell equations for analyzing the behavior of magnetization and/or contrast mechanism in CEST or APT MRI. We also present a method for analyzing the behavior of magnetization in spin-locking CEST MRI.

Keywords: Bloch-McConnell equations, numerical solution, chemical exchange saturation transfer (CEST) MRI, amide proton transfer (APT) MRI, spin-locking

1. Introduction

Chemical exchange saturation transfer (CEST) is one of the contrast mechanisms in magnetic resonance imaging (MRI) [1] and has been increasingly used to detect dilute proteins through the interaction between bulk water protons and labile solute protons [2–4]. Amide proton transfer (APT) MRI has been developed for imaging diseases such as acute stroke and cancer, and is now under intensive evaluation for clinical translation [5, 6]. APT MRI is a particular

type of CEST MRI that specifically probes labile amide protons of endogenous mobile proteins and peptides in tissue [5, 6]. In addition to APT MRI [5, 6], useful CEST MRI contrast for clinical imaging can be generated from amine protons [7], hydroxyl protons [8], glycosaminoglycans [9], and glutamate [10], as well as from changes in creatine and lactate concentrations [11]. Glucose and iopamidol have been used as exogenous CEST agents that have been administered to patients [12, 13]. Moreover, various CEST agents have been energetically developed to detect the parameters that reflect tissue molecular environment such as hydrogen ion exponent (pH) and/or to enhance the CEST effect [14].

In CEST or APT MRI, the exchangeable proton spins are saturated, and the saturation is transferred upon chemical exchange to the bulk water pool [1, 15]. As a result, a large contrast enhancement in bulk water can be achieved. The contrast mechanism of CEST or APT MRI, however, is complex and depends not only on the concentration of amide protons or CEST agents, relaxation, and exchange properties but also varies with imaging parameters such as radiofrequency (RF) power and magnetic field strength [15]. When there are multiple exchangeable pools within a single CEST system, the contrast mechanism of CEST becomes all the more complex [16]. Numerical simulations are useful and effective for analyzing the complex CEST contrast mechanism and for investigating the optimal imaging parameter values [17, 18]. In order to perform extensive numerical simulations for CEST or APT MRI, it requires the development of a simple and fast numerical method for obtaining the solutions to the time-dependent Bloch-McConnell equations.

In this chapter, we present the basics of CEST or APT MRI and a simple and fast numerical method for solving the time-dependent Bloch-McConnell equations for analyzing the behavior of magnetization and/or contrast mechanism in CEST or APT MRI. We also present it in SL CEST MRI.

2. Bloch-McConnell equations in the presence of CEST

2.1. Two-pool chemical exchange model

A two-pool chemical exchange model is illustrated in **Figure 1**. A and B in **Figure 1** represent the pools of bulk water protons and labile solute protons, respectively. The time-dependent Bloch-McConnell equations for the two-pool chemical exchange model in CEST or APT MRI are expressed as [17, 18].

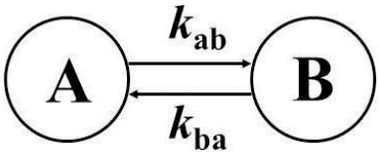

Figure 1. Two-pool chemical exchange model.

$$\begin{cases} \dfrac{dM_x^a(t)}{dt} = -R_2^a M_x^a(t) - k_{ab} M_x^a(t) + \Delta\omega_a M_y^a(t) - \omega_1^y M_z^a(t) + k_{ba} M_x^b(t) \\ \dfrac{dM_y^a(t)}{dt} = -\Delta\omega_a M_x^a(t) - R_2^a M_y^a(t) - k_{ab} M_y^a(t) + \omega_1^x M_z^a(t) + k_{ba} M_y^b(t) \\ \dfrac{dM_z^a(t)}{dt} = -\omega_1^y M_x^a(t) - \omega_1^x M_y^a(t) - R_1^a M_z^a(t) - k_{ab} M_z^a(t) + k_{ba} M_z^b(t) + R_1^a M_0^a \\ \dfrac{dM_x^b(t)}{dt} = k_{ab} M_x^a(t) - k_{ba} M_x^a(t) - R_2^b M_x^b(t) + \Delta\omega_b M_y^b(t) - \omega_1^y M_z^b(t) \\ \dfrac{dM_y^b(t)}{dt} = k_{ab} M_y^a(t) - \Delta\omega_b M_x^b(t) - R_2^b M_y^b(t) - k_{ba} M_y^b(t) + \omega_1^x M_z^b(t) \\ \dfrac{dM_z^b(t)}{dt} = k_{ab} M_z^a(t) + \omega_1^y M_y^b(t) - \omega_1^x M_y^b(t) - R_1^b M_z^b(t) - k_{ba} M_z^b(t) + R_1^b M_0^b \end{cases} \tag{1}$$

where superscripts a and b show the parameters in pool A and pool B, respectively. For example, $M_x^a(t)$, $M_y^a(t)$, and $M_z^a(t)$ are the x, y, and z magnetization components in pool A at time t, respectively. R_1^a and R_2^a are the reciprocals of the longitudinal (T_1^a) and transverse relaxation times (T_2^a), that is, the longitudinal and transverse relaxation rates in pool A, respectively. k_{ab} and k_{ba} denote the exchange rate from spins in pool A to those in pool B and that from spins in pool B to those in pool A, respectively (**Figure 1**). M_0^a and M_0^b are the thermal equilibrium z magnetization components in pool A and pool B, respectively. $\Delta\omega_a = \omega_a - \omega$ and $\Delta\omega_b = \omega_b - \omega$, where ω_a, ω_b, and ω denote the Larmor frequencies in pool A and pool B, and the frequency of the RF-pulse irradiation, respectively. ω_1^x and ω_1^y are the x and y components of the amplitude of the RF-pulse irradiation (ω_1), respectively. Note that $\omega_1 = \gamma B_1$, where γ and B_1 are the gyromagnetic ratio ($\gamma/2\pi = 42.58$ MH_z/T) and RF power, respectively. When the RF pulse is applied along an angle φ from the x-axis of the rotating frame as illustrated in **Figure 2**, ω_1^x and ω_1^y are represented by $\omega_1^x = \omega_1 \cos\phi$ and $\omega_1^y = \omega_1 \sin\phi$, respectively. When the RF pulse is applied along the x-axis of the rotating frame, ω_1^x and ω_1^y become ω_1 and 0, respectively.

The differential equations given by Eq. (1) can be combined into one vector equation (homogeneous linear differential equation) [18]:

$$\frac{d\mathbf{M}(t)}{dt} = \mathbf{A}(\omega, \omega_1, \phi) \cdot \mathbf{M}(t), \tag{2}$$

where

$$\mathbf{M}(t) = \begin{bmatrix} M_x^a(t) & M_y^a(t) & M_z^a(t) & M_x^b(t) & M_y^b(t) & M_z^b(t) & \mathbf{1} \end{bmatrix}^T \tag{3}$$

and

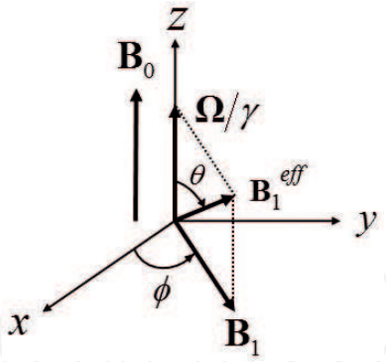

Figure 2. Parameters for analyzing the behavior of magnetization in the rotating frame.

$$\mathbf{A}(\boldsymbol{\omega}, \boldsymbol{\omega_1}, \boldsymbol{\phi}) = \begin{bmatrix} -\left(R_2^a + k_{ab}\right) & \Delta\omega_a & -\omega_1^y & k_{ba} & 0 & 0 & 0 \\ -\Delta\omega_a & -\left(R_2^a + k_{ab}\right) & \omega_1^x & 0 & k_{ba} & 0 & 0 \\ \omega_1^y & -\omega_1^x & -\left(R_1^a + k_{ab}\right) & 0 & 0 & k_{ba} & R_1^a M_0^a \\ k_{ab} & 0 & 0 & -\left(R_2^b + k_{ba}\right) & \Delta\omega_b & -\omega_1^y & 0 \\ 0 & k_{ab} & 0 & -\Delta\omega_b & -\left(R_2^b + k_{ba}\right) & \omega_1^x & 0 \\ 0 & 0 & k_{ab} & \omega_1^y & -\omega_1^x & -\left(R_1^b + k_{ba}\right) & R_1^b M_0^b \\ 0 & 0 & 0 & 0 & 0 & 0 & 0 \end{bmatrix}. \tag{4}$$

T in Eq. (3) denotes the matrix transpose.

For simplicity, we assume that the RF pulse is applied along the x-axis of the rotating frame, that is, $\phi = 0$. According to Koss et al. [19], the matrix $\mathbf{A}(\boldsymbol{\omega}, \boldsymbol{\omega}_1, 0)$ can be given by.

$$\mathbf{A}(\boldsymbol{\omega}, \boldsymbol{\omega_1}, 0) = \begin{bmatrix} \mathbf{E} & \mathbf{C} \\ \mathbf{0} & \mathbf{0} \end{bmatrix}, \tag{5}$$

where **E** is the evolution matrix and **C** is the constant-term matrix. Furthermore, **E** is given by.

$$\mathbf{E} = \mathbf{R} + \mathbf{K}. \tag{6}$$

In the case of **A** given by Eq. (4), **R** is reduced to.

$$\mathbf{R} = \begin{bmatrix} \mathbf{R^a} & \mathbf{0} \\ \mathbf{0} & \mathbf{R^b} \end{bmatrix}, \tag{7}$$

where

$$\mathbf{R}^a = \begin{bmatrix} -R_2^a & \Delta\omega_a & 0 \\ -\Delta\omega_a & -R_2^a & \omega_1 \\ 0 & -\omega_1 & R_1^a \end{bmatrix}, \tag{8}$$

and

$$\mathbf{R}^b = \begin{bmatrix} -R_2^b & \Delta\omega_b & 0 \\ -\Delta\omega_b & -R_2^b & \omega_1 \\ 0 & -\omega_1 & R_1^b \end{bmatrix}, \tag{9}$$

K in Eq. (6) is given by

$$\mathbf{K} = \begin{bmatrix} -k_{ab} & k_{ba} \\ k_{ab} & -k_{ba} \end{bmatrix} \otimes \mathbf{I}, \tag{10}$$

where **I** is a 3-by-3 identity matrix and ⊗ denotes the Kronecker tensor product. **C** in Eq. (5) is given by.

$$\mathbf{C} = \begin{bmatrix} R_1^a M_0^a & R_1^b M_0^b \end{bmatrix}^T \otimes \begin{bmatrix} 0 & 0 & 1 \end{bmatrix}^{\mathrm{T}}. \tag{11}$$

The solution of Eq. (2) with ϕ being 0 can be given by [18].

$$\mathbf{M}(t) = e^{\mathbf{A}(\omega,\omega_1,0)t}\mathbf{M}(0), \tag{12}$$

where t represents the so-called saturation time and **M**(0) is the matrix of initial values at $t = 0$. $e^{\mathbf{A}(\omega,\,\omega_1,\,0)t}$ is the matrix exponential.

It should be noted that mass balance imposes the following relationship between the exchange rates (k_{ab} and k_{ba}) of pool A and pool B [17]:

$$k_{ab} = (k_{ab} + k_{ba}) \cdot \frac{M_0^b}{M_0^a + M_0^b} \tag{13}$$

and

$$k_{ba} = (k_{ab} + k_{ba}) \cdot \frac{M_0^a}{M_0^a + M_0^b} \tag{14}$$

2.2. Three-pool chemical exchange model

Figure 3 illustrates a three-pool chemical exchange model in which pool a represents the bulk water pool. In this case, **R** and **K** are given by [19].

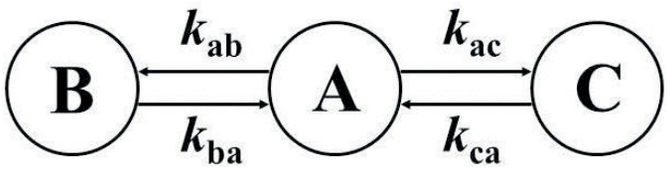

Figure 3. Three pool chemical exchange model.

$$\mathbf{R} = \begin{bmatrix} \boldsymbol{R^a} & 0 & 0 \\ 0 & \boldsymbol{R^b} & 0 \\ 0 & 0 & \boldsymbol{R^c} \end{bmatrix} \tag{15}$$

and

$$\mathbf{K} = \begin{bmatrix} -k_{ab} - k_{ac} & k_{ba} & k_{ca} \\ k_{ab} & -k_{ba} & 0 \\ k_{ac} & 0 & -k_{ac} \end{bmatrix} \otimes \mathbf{I}, \tag{16}$$

respectively. $\mathbf{R}^c$ in Eq. (15) is given by Eq. (8) in which the subscript *a* and superscript *a* are replaced by *c*. **C** is given by.

$$\mathbf{C} = \begin{bmatrix} R_{\mathbf{1}}^a M_0^a & R_{\mathbf{1}}^b M_0^b & R_{\mathbf{1}}^c M_0^c \end{bmatrix}^T \otimes \begin{bmatrix} \mathbf{0} & \mathbf{0} & \mathbf{1} \end{bmatrix}^T. \tag{17}$$

The solutions of other multi-pool chemical exchange models such as an hour-pool chemical exchange model are described in Ref. [20].

2.3. Calculation of Z-spectrum, MTR_{asym}, and PTR

The CEST effect has usually been analyzed using the so-called Z-spectrum [18]. The Z-spectrum is given by the following equation:

$$\mathrm{Z-spectrum} = \frac{M_z^a(\Delta\omega_{off})}{M_0^a}, \tag{18}$$

where $M_z^a(\Delta\omega_{off})$ is the z magnetization component of bulk water protons (pool A) at $\Delta\omega_{off}$. Note that $\Delta\omega_{off} = -\Delta\omega_a$.

The magnetization transfer asymmetry (MTR_{asym}) analysis has been performed using the following equation [18]:

$$\mathrm{MTR_{asym}} = \frac{M_z^a(-\Delta\omega_{off}) - M_z^a(\Delta\omega_{off})}{M_0^a}. \tag{19}$$

Instead of MTR_{asym}, the following equation for proton transfer ratio (PTR) has also been used for analyzing the CEST effect [18]:

$$\mathrm{PTR} = \frac{M_z^a(-\Delta\omega_{off}) - M_z^a(\Delta\omega_{off})}{M_z^a(-\Delta\omega_{off})}, \tag{20}$$

where $M_z^a(-\Delta\omega_{off})$ denotes the z magnetization component of pool A at the opposite side of the water resonance ($\Delta\omega_{off}$).

http://dx.doi.org/10.5772/intechopen.71645

Figure 4(a) shows Z-spectra as a function of offset frequency ($\Delta\omega_{off}$) for various saturation times (0.5, 1, 2, 5, and 10 s) in the two-pool chemical exchange model (**Figure 1**). **Figure 4(b)** shows Z-spectra as a function of $\Delta\omega_{off}$ for various ω_1 values (25, 50, 100, 150, and 200 Hz). It should be noted that because $B_1 = \omega_1/\gamma$, ω_1 values of 25, 50, 100, 150, and 200 Hz correspond to B_1 values of 0.59, 1.17, 2.35, 3.52, and 4.70 μT, respectively. **Figure 4(c)** shows Z-spectra as a function of $\Delta\omega_{off}$ for various M_0^b/M_0^a values (1/500, 1/250, 1/125, 1/100, and 1/50).

In the above simulations, we assumed that T_1^a and T_2^a were 3 s and 100 ms, respectively, and $T_1^b = 1$ s and $T_2^b = 15$ ms [16]. The chemical shift of protons in pool B was set to be 4 ppm. It should be noted that the chemical shift of 4 ppm corresponds to $\Delta\omega_{off}$ of 1192.8 Hz for the magnetic field strength of 7 T. Unless otherwise indicated, $k_{ab} + k_{ba}$ was assumed to be 100 Hz. M_0^a and M_0^b were assumed to be 1 and 1/250, respectively. The saturation time and ω_1 were taken as 2 s and 100 Hz, respectively. The matrix exponential and Kronecker tensor product were calculated using the MATLAB® functions "expm" and "kron," respectively.

The peaks at 0 Hz (0 ppm) and 1192.8 Hz (4 ppm) in **Figure 4** derived from pool A and pool B, respectively. As shown in **Figure 4(a)** and **Figure 4(b)**, Z-spectra changed largely depending on the saturation time and ω_1, that is, Z-spectra became broad and tended to saturate with increasing saturation time and ω_1. As shown in **Figure 4(c)**, the peaks at 1192.8 Hz increased with increasing M_0^b/M_0^a value.

Figure 5 shows cases for the three-pool chemical exchange model (**Figure 3**) consisting of bulk water (pool A) and two labile proton pools (pool B and pool C). In these cases, we assumed that $T_1^a = 3\ s$, $T_2^a = 100\ ms$, $T_1^b = T_1^c = 1$ s, and $T_2^b = T_2^c = 15$ ms [16]. The chemical shifts of two labile proton pools were set to be 4 ppm ($\Delta\omega_{off}$=1192.8 Hz for the magnetic field strength of 7 T) and 5 ppm ($\Delta\omega_{off}$=1491.0 Hz for 7 T). Unless otherwise indicated, $k_{ab} + k_{ba}$, $k_{ac} + k_{ca}$, and $k_{bc} + k_{cb}$ were assumed to be 100 Hz, 300 Hz, and 100 Hz, respectively. M_0^a, M_0^b, and M_0^c were assumed to be 1, 1/250, and 1/500, respectively. The saturation time and ω_1 were taken as 5 s and 50 Hz, respectively.

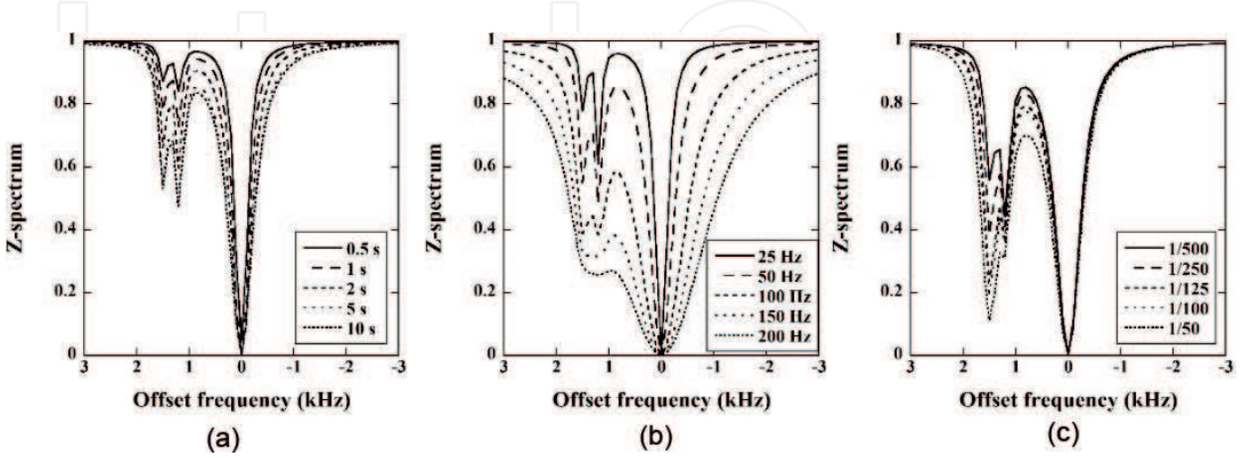

Figure 4. Z-spectra as a function of $\Delta\omega_{off}$ for various values of saturation time (a), ω_1 (b), and M_0^b/M_0^a (c) in the two-pool chemical exchange model.

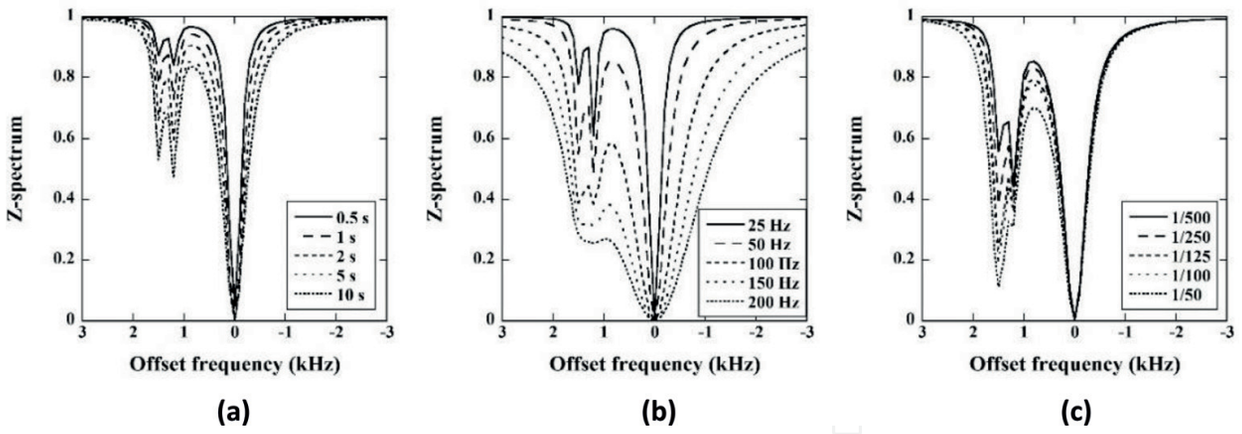

Figure 5. Z-spectra as a function of $\Delta\omega_{off}$ for various values of saturation time (a), ω_1 (b), and M_0^c/M_0^a (c) in the three-pool chemical exchange model.

Figure 5(a) shows Z-spectra as a function of $\Delta\omega_{off}$ for various saturation times (0.5, 1, 2, 5, and 10 s). The peaks at 0 Hz (0 ppm), 1192.8 Hz (4 ppm), and 1491.0 Hz (5 ppm) derive from pool A, pool B, and pool C, respectively. As shown in **Figure 5(a)**, Z-spectra changed largely depending on the saturation time, that is, Z-spectra became broad and tended to saturate with increasing saturation time. **Figure 5(b)** shows Z-spectra as a function of $\Delta\omega_{off}$ for various ω_1 values (25, 50, 100, 150, and 200 Hz). As in **Figure 4(b)**, Z-spectra became broad with increasing ω_1 value. **Figure 5(c)** shows Z-spectra as a function of $\Delta\omega_{off}$ for various M_0^c/M_0^a values (1/500, 1/250, 1/125, 1/100, and 1/50). The peaks at 1491.0 Hz increased with increasing M_0^c/M_0^a value.

Figure 6(a) shows the MTR_{asym} values given by Eq. (19) as a function of ω_1 for various saturation times (0.5, 1, 2, 5, and 10 s) in the two-pool chemical exchange model (**Figure 1**), whereas **Figure 6(b)** shows those as a function of saturation time for various ω_1 values (25, 50, 100, 150, and 200 Hz). As shown in **Figure 6(a)**, when ω_1 was small, MTR_{asym} tended to

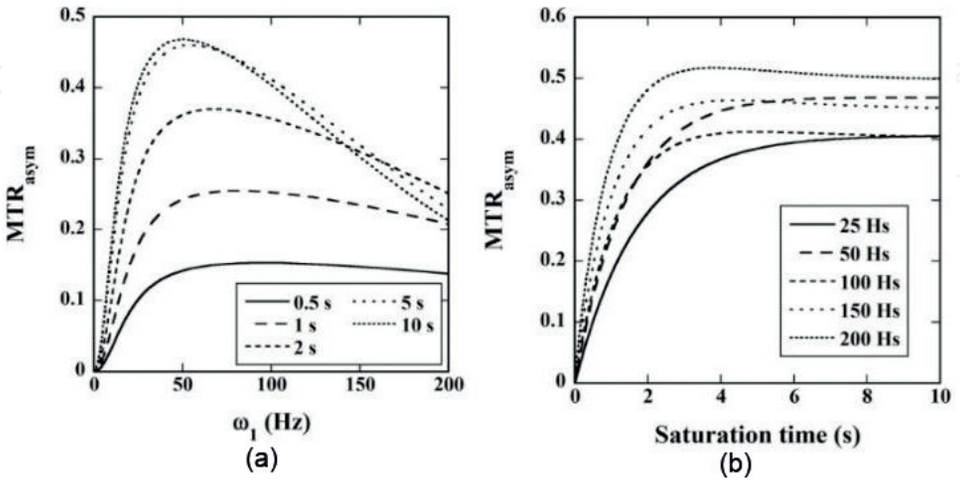

Figure 6. (a) MTR_{asym} values as a function of ω_1 for various saturation times in the two – pool chemical exchange model. (b) MTRasym values as a function of saturation time for various ω_1 values.

http://dx.doi.org/10.5772/intechopen.71645

increase with increasing ω_1 and saturation time. However, when ω_1 was large, MTR_{asym} tended to saturate or decrease with increasing ω_1 value, depending on the saturation time. As shown in **Figure 6(b)**, MTR_{asym} tended to saturate with increasing saturation time for all ω_1 values.

Figure 7(a) shows the PTR values given by Eq. (20) as a function of ω_1 for various saturation times (0.5, 1, 2, 5, and 10 s) in the two-pool chemical exchange model (**Figure 1**), whereas **Figure 7(b)** shows those as a function of saturation time for various ω_1 values (25, 50, 100, 150, and 200 Hz). As shown in **Figure 7**, although PTR showed almost the same tendency with MTR_{asym} (**Figure 6**), the change in the PTR value depending on the saturation time or ω_1 was larger than that in the MTR_{asym} value.

In this study, we presented a simple equation for solving the time-dependent Bloch-McConnell equations, in which our previous method [18] and the approach presented by Koss et al. [19] were combined. Our method can be easily expanded to multi-pool chemical exchange models by modifying the matrix **A** in Eq. (2). We previously reported that the solutions obtained by our method agreed with the analytical solutions given by Mulkern and Williams, [21] and the numerical solutions obtained using a fourth/fifth-order Runge–Kutta-Fehlberg (RKF) algorithm [18], indicating the validity of our method. In addition, our method considerably reduced the computation time as compared with the RKF algorithm [18]. These results suggest that our method will be useful in calculating the parameters such as the exchange rate of CEST agents using the non-linear least-squares fitting method [17].

As previously described, the so-called Z-spectrum has usually been used to analyze the CEST effect [18]. The Z-spectrum is obtained by plotting the z magnetization component of bulk water protons (M_z^a) in the form of M_z^a versus $\Delta\omega_{off}$ [Eq. (18)]. **Figure 4(a)** and **Figure 5(a)** showed that the saturation time affected the Z-spectra, and the CEST effect increased and saturated with increasing saturation time. The fact that the CEST effect saturates with increasing saturation time is more clearly confirmed by the relationship between MTR_{asym} or PTR,

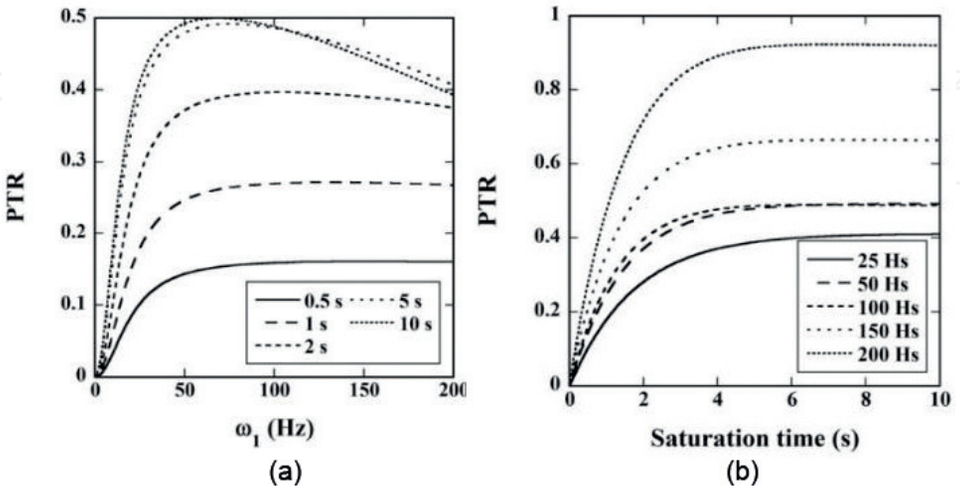

Figure 7. (a) PTR values as a function of ω_1 for various saturation times in the two – pool chemical exchange model. (b) PTR values as a function of saturation time for various ω_1 values.

and the saturation time shown in **Figure 6(b)** or **Figure 7(b)**. As shown in **Figure 4(b)** and **Figure 5(b)**, ω_1 also affected the Z-spectra. Although the CEST effect increased with increasing ω_1 value, the separation among peaks in the Z-spectrum plots degraded with increasing ω_1 value. The influence of ω_1 on the CEST effect is also clearly demonstrated by the relationship between MTR_{asym} and PTR, and ω_1 shown in **Figure 6(a)** or **Figure 7(a)**. The use of large ω_1 may directly saturate bulk water protons, causing the so-called spillover effect [18]. The results shown in **Figures 4–7** suggest that the values of imaging parameters in CEST MRI such as the saturation time and ω_1 must be determined in consideration of both the CEST effect and spillover effect. Our method is useful for determining the optimal values of imaging parameters in CEST MRI.

2.4. Calculation of $R_{1\rho}$ and $R_{2\rho}$

The longitudinal relaxation rate in the rotating frame ($R_{1\rho}$) can be obtained from the negative of the largest (least negative) real eigenvalue (λ_1) of the matrix **A** in Eq. (2), that is, $R_{1\rho} = -\lambda_1$ [19, 22].

The transverse relaxation rate in the rotating frame ($R_{2\rho}$) can be obtained from the absolute value of the largest real part of the complex eigenvalue (λ_2) of the matrix **A** in Eq. (2), that is, $R_{2\rho} = |\mathrm{Re}(\lambda_2)|$ [22], where Re denotes the real part of a complex number.

Figure 8 shows the common logarithm of $R_{1\rho}$ (a) and $R_{2\rho}$ (b) as a function of $\Delta\omega_{off}$ for saturation times of 0.5, 1, 2, 5, and 10 s in the two-pool chemical exchange model (**Figure 1**). The peaks at 0 Hz (0 ppm) and 1192.8 Hz (4 ppm) derive from pool A and pool B, respectively. As shown in **Figure 8**, $R_{1\rho}$ and $R_{2\rho}$ were not affected by the saturation time.

Figure 9 shows the common logarithm of $R_{1\rho}$ (a) and $R_{2\rho}$ (b) as a function of $\Delta\omega_{off}$ for ω_1 values of 25, 50, 100, 150, and 200 Hz in the two-pool chemical exchange model (**Figure 1**). As shown in **Figure 9**, both parameters became broad with increasing ω_1 value.

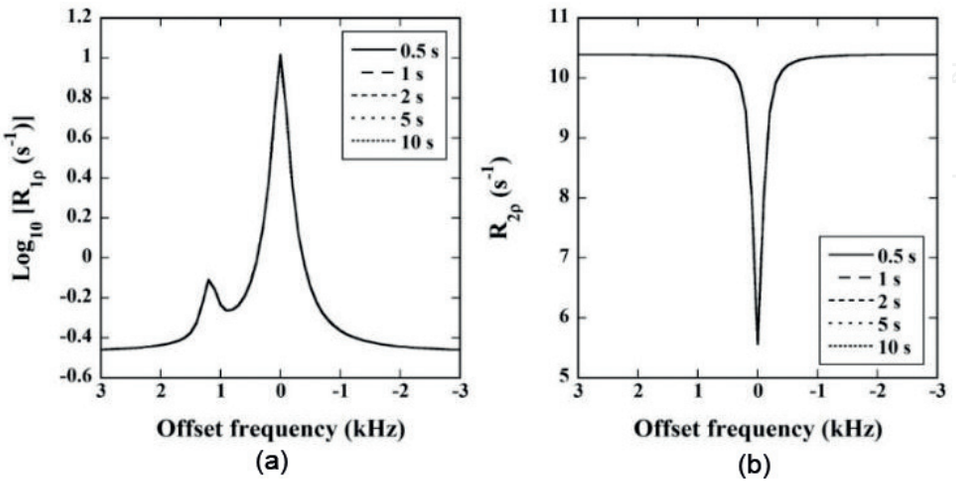

Figure 8. (a) Common logarithm of $R_{1\rho}$ and (b) $R_{2\rho}$ values as a function of $\Delta\omega_{off}$ for various saturation times in the two-pool chemical exchange model.

http://dx.doi.org/10.5772/intechopen.71645

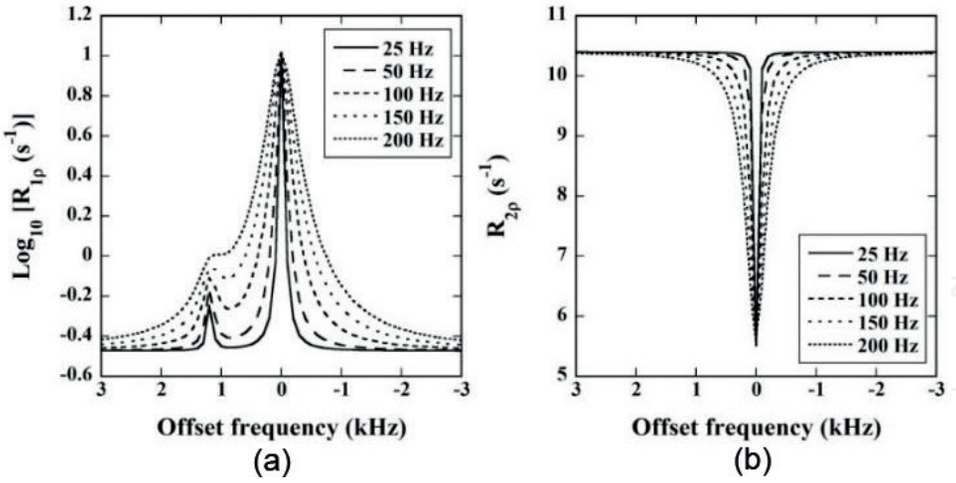

Figure 9. (a) Common logarithm of $R_{1\rho}$ and (b) $R_{2\rho}$ values as a function of $\Delta\omega_{off}$ for various ω_1 values in the two-pool chemical exchange model.

As described above, $R_{1\rho}$ and $R_{2\rho}$ can be obtained from the negative of the largest (least negative) real eigenvalue and the absolute value of the largest real part of the complex eigenvalue of the matrix **A** in Eq. (2), respectively. We previously reported that there was good agreement between the $R_{1\rho}$ and $R_{2\rho}$ values thus obtained and those obtained numerically [22]. These results appear to indicate the validity of these procedures.

As shown in **Figure 8**, $R_{1\rho}$ and $R_{2\rho}$ were not affected by the saturation time, because the matrix **A** in Eq. (2) is independent of the saturation time. When ω_1 was varied, the influence of ω_1 on $R_{1\rho}$ and $R_{2\rho}$ increased with increasing ω_1 value (**Figure 9**). Especially, the separation between peaks in the $R_{1\rho}$ plots degraded with increasing ω_1 value [**Figure 9(a)**]. This also appears to be due to the spillover effect.

3. Spin-locking CEST MRI

3.1. Principle of spin-locking

Longitudinal relaxation time in the rotating frame ($T_{1\rho}$) has been demonstrated to be effective for probing the slow-motion interactions between motion-restricted water molecules and their local macromolecular environment [23] and provides novel image contrast that is not available from conventional MRI techniques. The imaging of biologic tissue based on $T_{1\rho}$ is currently being investigated for various tissues, including articular cartilage, breast, and head and neck [24–26]. In $T_{1\rho}$-weighted MRI of tissues, the image is sensitive to molecular processes that occur over a range of frequencies determined by the amplitude of an applied SL pulse [23].

As pointed out by Jin et al. [27], the SL approach is useful for improving the signal-to-noise ratio (SNR) in CEST MRI. Furthermore, Kogan et al. [28] demonstrated that a combination of the CEST and SL approaches is useful for detecting proton exchange in the slow-to intermediate-exchange regimes.

As earlier described, the Bloch-McConnell equations for the two-pool chemical exchange model (**Figure 1**) in the rotating frame with the same frequency as that of the RF-pulse irradiation is given by Eq. (2) [18, 29]. The solution of Eq. (2) can be given by [18]

$$\mathbf{M}(t) = e^{\mathbf{A}(\omega,\omega_1,\phi)t}\mathbf{M}(0). \tag{21}$$

Figure 10 illustrates the image of the pulse sequence with SL. We assume that the SL pulse (frequency: ω, amplitude: ω_1, and frequency offset: Ω) is applied on the x-axis (**Figure 2**). The effective magnetic field (B_1^{eff}) and its angle with respect to the z − axis (θ) are given by $B_1^{eff} = \sqrt{\omega_1^2 + \Omega^2}/\gamma$ and $\theta = \tan^{-1}(\omega_1/\Omega)$, respectively (**Figure 2**). To achieve SL, the magnetization is first flipped by the θ-degree RF pulse (frequency: ω and amplitude: ω_1^θ) to the x-z plane, then spin locked by B_1^{eff} for a duration of t_{SL}, and then flipped back to the z-axis for imaging (**Figure 10**). The θ-degree RF pulse for flipping is applied on the –y axis, that is, $\phi = -\pi/2$, whereas the θ-degree RF pulse for flipping back is applied on the y axis, that is, $\phi = \pi/2$. The θ-degree rotation matrix for flipping [$\mathbf{R}(\theta)$] is given by [30].

$$\mathbf{R}(\theta) = e^{\mathbf{A}\left(\omega_a,\omega_1^\theta,-\pi/2\right)t_\theta}, \tag{22}$$

where ω_1^θ and t_θ denote the amplitude and the duration of the θ-degree RF-pulse irradiation, respectively (**Figure 10**), and $\omega_1^\theta \times t_\theta = \theta$. Thus, we obtain the magnetization vector immediately after SL for a duration of t_{SL} [$\mathbf{M}^-(t_{SL})$] as.

$$\mathbf{M}^-(t_{SL}) = e^{\mathbf{A}(\omega,\omega_1,0)t_{SL}}\mathbf{R}(\theta)\mathbf{M}(0). \tag{23}$$

The θ-degree rotation matrix for flipping back to the z-axis [$\mathbf{R}(-\theta)$] is given by.

$$\mathbf{R}(-\theta) = e^{\mathbf{A}\left(\omega_a,\omega_1^\theta,\pi/2\right)t_\theta}, \tag{24}$$

Thus, the magnetization vector after flipping back to the z-axis [$\mathbf{M}^+(t_{SL})$] is given by.

$$\mathbf{M}^+(t_{SL}) = \mathbf{R}(-\theta)\mathbf{M}^-(t_{SL}) = \mathbf{R}(-\theta)e^{\mathbf{A}(\omega,\omega_1,0)t_{SL}}\mathbf{R}(\theta)\mathbf{M}(0). \tag{25}$$

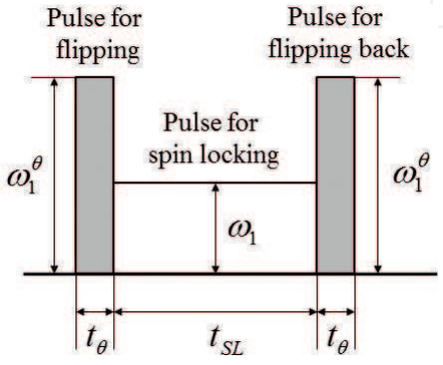

Figure 10. Diagram of spin-locking pulse sequence.

Note that Ω and θ are taken to be 0 and π/2, respectively, for an on-resonance SL sequence, whereas the saturation pulse is applied without flipping the magnetization in the sequence without SL such as the conventional CEST sequence [15]. Therefore, the magnetization vector after the saturation pulse [$\mathbf{M}(t_{SAT})$] in the conventional CEST MRI is simply expressed as.

$$\mathbf{M}(t_{SAT}) = e^{\mathbf{A}(\boldsymbol{\omega},\boldsymbol{\omega_1},0)t_{SAT}}\mathbf{M}(0), \tag{26}$$

where t_{SAT} denotes the duration of saturation.

3.2. Calculation of $T_{1\rho}$

$T_{1\rho}$ can be obtained numerically by fitting the z component of magnetization for t_{SL} [$\mathbf{M}^{+}(t_{SL})$ given by Eq. (25)] in pool A [$M_z^a(t_{SL})$] to the following equation [30]:

$$M_z^a(t_{SL}) = \left(M_0^a - M_{zss}^a\right)e^{-t_{SL}/T_{1\rho}} + M_{zss}^a, \tag{27}$$

where M_{zss}^a denotes the steady-state z component of magnetization in pool A. In this study, we used the Simplex method [31] to calculate $T_{1\rho}$ from Eq. (27).

The approximate solution for $T_{1\rho}$ has been derived by Trott and Palmer [29]:

$$T_{\mathbf{1}\rho} \approx \frac{\mathbf{1}}{R_{\mathbf{1}}\cos^{\mathbf{2}}\theta + (R_{\mathbf{2}} + R_{ex})\sin^{\mathbf{2}}\theta}, \tag{28}$$

where $\theta = \tan^{-1}(\omega_1/\Omega)$, $R_{ex} = P_aP_b\Delta\omega^2k_{ex}/\left(\omega_{ae}^2\omega_{be}^2/\omega_e^2 + k_{ex}^2\right)$, $\omega_{ae} = \sqrt{\omega_1^2 + \Delta\omega_a^2}$, $\omega_{be} = \sqrt{\omega_1^2 + \Delta\omega_b^2}$, $\omega_e = \sqrt{\omega_1^2 + \Omega^2}$, $\Omega = \overline{\omega} - \omega$, $\overline{\omega} = P_a\omega_a + P_b\omega_b$, $\Delta\omega = \Delta\omega_b - \Delta\omega_a = \omega_b - \omega_a$, and $k_{ex} = k_{ab} + k_{ba}$. P_a and P_b are the fractional sizes of pool A and pool B, and are given by $P_a = M_0^a/\left(M_0^a + M_0^b\right)$ and $P_b = M_0^b/\left(M_0^a + M_0^b\right)$, respectively. R_1 and R_2 are the population-averaged relaxation rates, and are given by $R_1 = P_aR_1^a + P_bR_1^b$ and $R_2 = P_aR_2^a + P_bR_2^b$, respectively. It should be noted that Ω is the population-averaged offset frequency in this case. M_{zss}^a in Eq. (27) is approximated by [27].

$$\frac{M_{zss}^a}{M_0^a} \approx \frac{R_{\mathbf{1}}\cos^{\mathbf{2}}\theta}{R_{\mathbf{1}\rho}}. \tag{29}$$

Figure 11 shows an example of the three-dimensional plots of the magnetization vector in pool A in the two-pool chemical exchange model (**Figure 1**). **Figure 11(a)** and **11(b)** show cases without and with SL, respectively. In these cases, the relaxation time constants were assumed to be $T_1^a = 1.5$ s, $T_2^a = 0.06$ s, $T_1^b = 0.77$ s, and $T_2^b = 0.033$ s [32]. t_θ in Eq. (22) and (24) was taken as 200 μs [27]. ω_1^θ in Eq. (22) and (24) was calculated from $\omega_1^\theta = \theta/t_\theta$. Unless specifically stated, $\Delta\omega$ ($=\omega_b - \omega_a$) and ω_1 were assumed to be 2400 and 1000 Hz, respectively. Ω was assumed to be 2000 Hz. Thus, θ was $\tan^{-1}(\omega_1/\Omega) = \tan^{-1}(1000/2000) \approx 26.6$ degrees. k_{ex} ($=k_{ab}+k_{ba}$) was assumed to be 1500 Hz, and k_{ab} was assumed to be given by $k_{ab} = \left(M_0^b/M_0^a\right)k_{ba}$ [18]. M_0^b/M_0^a was assumed to be 0.03. As shown in **Figure 11(a)**, when the SL pulse was not applied, the magnetization vector rotated largely around B_1^{eff}. On the other hand, when the SL pulse was

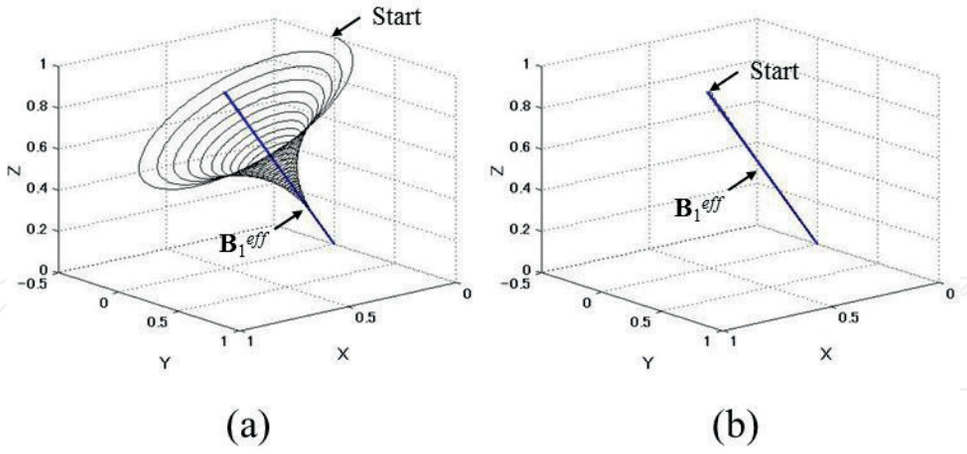

Figure 11. Three-dimensional plots of the magnetization vector in pool A in the two-pool chemical exchange model. (a) and (b) show cases without and with spin-locking pulse, respectively.

applied [**Figure 11(b)**], the magnetization vector moved along B_1^{eff}, and the rotation around B_1^{eff} was suppressed.

When M_0^b/M_0^a was 0.003, there was good agreement between the $T_{1\rho}$ values calculated from Eq. (27) and Trott and Palmer's solutions given by Eq. (28) (data not shown). When M_0^b/M_0^a was 0.03, some difference was observed between them in the off-resonance case. When M_0^b/M_0^a was 0.3, large differences were observed between them in both the on- and off-resonance cases [30].

In this study, we developed a simple and fast method for calculating the magnetization vector in SL CEST MRI, in which a simple matrix equation was derived for solving the time-dependent Bloch-McConnell equations in SL MRI [Eq. (25)] and the θ-degree rotation matrix [Eq. (22)] was introduced for considering the effect of the θ-degree RF pulse for flipping the magnetization. As shown in **Figure 11**, the trajectory of the magnetization vector in the sequence with SL could be visualized by calculating $\mathbf{M}^-(t_{SL})$ using Eq. (23), whereas that in the sequence without SL could be visualized by calculating $\mathbf{M}(t_{SAT})$ using Eq. (26). Although **Figure 11** shows the three-dimensional plots observed from one direction, we can observe the trajectory of the magnetization vector from various directions by rotating the plot. If we compared the three-dimensional plots with and without SL (**Figure 11**), then the effect of SL is well understood. Therefore, our method is helpful for visually understanding the effect of SL. In addition, as our method allows us to simply and quickly calculate the time evolution of the magnetization vector under various study conditions in SL CEST MRI, our method can also be useful for optimizing the study conditions in SL CEST MRI.

As previously described, when M_0^b/M_0^a was small, that is, when the population of two pools was highly asymmetric, the $T_{1\rho}$ values calculated from Eq. (27) agreed with the solutions given by Eq. (28). However, the difference between them increased with increasing M_0^b/M_0^a [30]. This finding appears to be due to the fact that Trott and Palmer's solution [Eq. (28)] was derived by approximating the parameters such as relaxation rates using their population-averaged values, and thus the validity of this approximation decreases with decreasing asymmetry in the populations of the two pools.

Although we treated the two-pool chemical exchange model (**Figure 1**) for analyzing $T_{1\rho}$ or $R_{1\rho}$ in SL CEST MRI, recent investigations have shown the importance of improved theoretical approaches for describing multi-site chemical exchange phenomena [33, 34]. Thus, Trott and Palmer [33] have tried to generalize their approach for $T_{1\rho}$ or $R_{1\rho}$ [29]. For such purposes, it is necessary to expand the Bloch-McConnell equations to those based on multi-pool chemical exchange models. Our method can be easily expanded to multi-pool chemical exchange models by modifying the matrix **A** given by Eq. (4) [20] as previously described, and it is helpful for testing the validity of newly developed approaches for analyzing multi-site chemical exchange phenomena.

4. Correction of B_0 and B_1

As previously described, the CEST effect has usually been analyzed using MTR_{asym} [Eq. (19)] or PTR [Eq. (20)]. However, these parameters are susceptible to the B_0 inhomogeneity of the static magnetic field. When there exists the B_0 inhomogeneity, the spillover effect is no longer symmetric. Furthermore, the B_1 inhomogeneity of the RF pulse may also cause spatial variation in labeling efficiency and spillover factor [35]. Apart from the efforts in improving magnetic field inhomogeneities using hardware-based methods, such as parallel transmit technologies [36], post-processing algorithms have been developed for field inhomogeneity correction [37, 38].

Kim et al. [37] showed that direct water saturation imaging allows measurement of the absolute water frequency in each voxel, allowing proper centering of Z-spectra on a voxel-by-voxel basis independent of spatial B_0 field variations, and that the B_0 inhomogeneity in CEST MRI can be corrected on a voxel-by-voxel basis through the centering of Z-spectra. This method is called "water saturation shift referencing (WASSR)" approach. This method, however, would require acquisition of saturation images at 20–40 frequencies [38]. Since the SNR of CEST MRI is low, multiple acquisitions for each frequency offset of complete *Z*-spectra would be needed, which is not practical in the clinical setting. Zhou et al. demonstrated that a practical six-offset multi-acquisition method combined with a single reference *Z*-spectrum to acquire high-SNR CEST MRI can accomplish improved CEST MRI with B_0 inhomogeneity correction within an acceptable scanning time [38].

A B_1-correction of CEST contrasts is crucial for the evaluation of data obtained in clinical studies at high field strengths with strong B_1-inhomogeneities. To correct for the B_1 inhomogeneity, a B_1 map is acquired for correction of Z-spectra using either a calibration [39] or an interpolation approach [40]. Singh et al. [39] developed an approach for B_1 inhomogeneity correction based on acquiring calibration data at a coarsely sampled B_1 values in conjunction with the measured B_1 maps, whereas Windschuh et al. [40] developed an approach based on Lorentzian line fits.

The comprehensive methods like simultaneous mapping of B_0 and B_1 fields [35, 41], and model-based correction algorithm, [42] have also been developed to improve the accuracy of MTR_{asym} or PTR.

Acknowledgements

This work was supported, in part, by a Grant-in-Aid for Challenging Exploratory Research (Grant No. 25670532) from the Japan Society for the Promotion of Science.

Author details

Kenya Murase

Address all correspondence to: murase@sahs.med.osaka-u.ac.jp

Department of Medical Physics and Engineering, Division of Medical Technology and Science, Faculty of Health Science, Graduate School of Medicine, Osaka University, Osaka, Japan

References

[1] Ward K, Aletras A, Balaban R. A new class of contrast agents for MRI based on proton chemical exchange dependent saturation transfer (CEST). Journal of Magnetic Resonance. 2000;**143**:79-87

[2] Goffeney N, Bulte JWM, Duyn J, Bryant LH, van Zijl PCM. Sensitive NMR detection of cationic-polymer-based gene delivery systems using saturation transfer via proton exchange. Journal of the American Chemical Society. 2001;**123**:8628-8629

[3] Aime S, Barge A, Delli Castelli D, Fedeli F, Mortillaro A, Nielsen FU, Terreno E. Paramagnetic lanthanide (III) complexes as pH-sensitive chemical exchange saturation transfer (CEST) contrast agents for MRI applications. Magnetic Resonance in Medicine. 2002; **47**:639-648

[4] Snoussi K, Bulte JWM, Gueron M, van Zijl PCM. Sensitive CEST agents based on nucleic acid imino proton exchange: Detection of poly(rU) and of a dendrimer-poly(rU) model for nucleic acid delivery and pharmacology. Magnetic Resonance in Medicine. 2003;**49**: 998-1005

[5] Zhou J, Lal B, Wilson DA, Laterra J, van Zijl PCM. Amide proton transfer (APT) contrast for imaging of brain tumors. Magnetic Resonance in Medicine. 2003;**50**:1120-1126

[6] Sun PZ, Murata Y, Lu J, Wang X, Lo EH, Sorensen AG. Relaxation-compensated fast multislice amide proton transfer (APT) imaging of acute ischemic stroke. Magnetic Resonance in Medicine. 2008;**59**:1175-1182

[7] Harris RJ, Cloughesy TF, Liau LM, Prins RM, Antonios JP, Li D, Yong WH, Pope WB, Lai A, Nghiemphu PL, Ellingson BM. pH-weighted molecular imaging of gliomas using amine chemical exchange saturation transfer MRI. Neuro Oncol. 2015;**17**:1514-1524

[8] Van Zijl PCM, Jones CK, Ren J, Malloy CR, Sherry AD. MRI detection of glycogen *in vivo* by using chemical exchange saturation transfer imaging (glycoCEST). Proceedings of the National Academy of Sciences of the United States of America. 2007;**104**:4359-4364

[9] Ling W, Regatte RR, Navon G, Jerschow A. Assessment of glycosaminoglycan concentration in vivo by chemical exchange-dependent saturation transfer (gagCEST). Proceedings of the National Academy of Sciences of the United States of America. 2008;**105**: 2266-2270

[10] Cai K, Haris M, Singh A, Kogan F, Greenberg JH, Hariharan H, Detre JA, Reddy R. Magnetic resonance imaging of glutamate. Nature Medicine. 2012;**18**:302-306

[11] Jones KM, Pollard AC, Pagel MD. Clinical applications of chemical exchange saturation transfer (CEST) MRI. Journal of Magnetic Resonance Imaging. 2017 (in press)

[12] Walker-Samuel S, Ramasawmy R, Torrealdea F, Rega M, Rajkumar V, Johnson SP, Richardson S, Gonçalves M, Parkes HG, Arstad E, Thomas DL, Pedley RB, Lythgoe MF, Golay X. In vivo imaging of glucose uptake and metabolism in tumors. Nature Medicine. 2013;**19**:1067-1072

[13] Chen LQ, Howison CM, Jeffery JJ, Robey IF, Kuo PH, Pagel MD. Evaluations of extracellular pH within in vivo tumors using acidoCEST MRI. Magnetic Resonance in Medicine. 2014;**72**:1408-1417

[14] Maruyama S, Ueda J, Kimura A, Murase K. Development and characterization of novel LipoCEST agents based on thermosensitive liposomes. Magnetic Resonance in Medical Sciences. 2016;**15**:324-334

[15] Sun PZ. Simultaneous determination of labile proton concentration and exchange rate utilizing optimal RF power: Radio frequency power (RFP) dependence of chemical exchange saturation transfer (CEST) MRI. Journal of Magnetic Resonance. 2010;**202**: 155-161

[16] Sun PZ. Simplified and scalable numerical solution for describing multi-pool chemical exchange saturation transfer (CEST) MRI contrast. Journal of Magnetic Resonance. 2010;**205**: 235-241

[17] Woessner DE, Zhang S, Merritt ME, Sherry AD. Numerical solution of the Bloch equations provides insights into the optimum design of PARACEST agents for MRI. Magnetic Resonance in Medicine. 2005;**53**:790-799

[18] Murase K, Tanki N. Numerical solutions to the time-dependent Bloch equations revisited. Magnetic Resonance Imaging. 2011;**29**:126-131

[19] Koss H, Rance M, Palmer AG. General expression for $R_1\rho$ relaxation for *N*-site chemical exchange and the special case of linear chains. Journal of Magnetic Resonance. 2017;**274**:36-45

[20] Murase K. Numerical analysis of the magnetization behavior in magnetic resonance imaging in the presence of multiple chemical exchange pools. Open Journal of Applied Sciences. 2017;**7**:1-14

[21] Mulkern RV, Williams ML. The general solution to the Bloch equation with constant rf and relaxation terms: Application to saturation and slice selection. Medical Physics. 1993;**20**:5-13

[22] Murase K. A theoretical and numerical consideration of the longitudinal and transverse relaxations in the rotating frame. Magnetic Resonance Imaging. 2013;**31**:1544-1558

[23] Li X, Han ET, Busse RF, Majumdar S. *In vivo* $T_1\rho$ mapping in cartilage using 3D magnetization prepared angle-modulated partitioned *k*-space spoiled gradient echo snapshots (3D MAPSS). Magnetic Resonance in Medicine. 2008;**59**:298-307

[24] Regatte RR, Akella SV, Borthakur A, Kneeland JB, Reddy R. *In vivo* proton MR three-dimensional $T_1\rho$ mapping of human articular cartilage: Initial experience. Radiology. 2003;**229**:269-274

[25] Santyr GE, Henkelman RM, Bronskill MJ. Spin locking for magnetic resonance imaging with application to human breast. Magnetic Resonance in Medicine. 1989;**12**:25-37

[26] Markkola AT, Aronen HJ, Paavonen T, Hopsu E, Sipila LM, Tanttu JI, Sepponen RE. Spin lock and magnetization transfer imaging of head and neck tumors. Radiology. 1996;**200**:369-375

[27] Jin T, Autio J, Obata T, Kim S-G. Spin-locking versus chemical exchange saturation transfer MRI for investigating chemical exchange process between water and labile metabolite protons. Magnetic Resonance in Medicine. 2011;**65**:1448-1460

[28] Kogan F, Singh A, Cai K, Haris M, Hariharan H, Reddy R. Investigation of chemical exchange at intermediate exchange rates using a combination of chemical exchange saturation transfer (CEST) and spin-locking methods (CESTrho). Magnetic Resonance in Medicine. 2012;**68**:107-119

[29] Trott O, Palmer AG. $R1\rho$ relaxation outside of the fast-exchange limit. Journal of Magnetic Resonance. 2002;**154**:157-160

[30] Murase K. Behavior of the magnetization in spin-locking magnetic resonance imaging using numerical solutions to the time-dependent Bloch equations. Physics in Medicine and Biology. 2012;**57**:N481-N492

[31] Nelder JA, Mead R. A simplex method for function minimization. The Computer Journal. 1965;**7**:308-313

[32] Sun PZ, Zhou J, Huang J, van Zijl P. Simplified quantitative description of amide proton transfer (APT) imaging during acute ischemia. Magnetic Resonance in Medicine. 2007;**57**: 405-410

[33] Trott O, Palmer AG. Theoretical study of $R_{1\rho}$ rotating-frame and R_2 free-precession relaxation in the presence of n-site chemical exchange. Journal of Magnetic Resonance. 2004;**170**:104-112

[34] Grey MJ, Wang C, Palmer AG. Disulfide bond isomerization in basic pancreatic trypsin inhibitor: Multisite chemical exchange quantified by CPMG relaxation dispersion and chemical shift modeling. Journal of the American Chemical Society. 2003;**125**:14324-14335

[35] Ji Y, Zhou IY, Qiu B, Sun PZ. Progress toward quantitative in vivo chemical exchange saturation transfer (CEST) MRI. Israel Journal of Chemistry. 2017;**57**:1-17

[36] Padormoa F, Beqiria A, Hajnalab JV, Malika SJ. Parallel transmission for ultrahigh-field imaging. NMR in Biomedicine. 2016;**29**:1145-1161

[37] Kim M, Gillen J, Landman BA, Zhou J, Van Zijl PC. Water saturation shift referencing (WASSR) for chemical exchange saturation transfer (CEST) experiments. Magnetic Resonance in Medicine. 2009;**61**:1441-1450

[38] Zhou J, Blakeley JO, Hua J, Kim M, Laterra J, Pomper MG, Van Zijl PC. Practical data acquisition method for human brain tumor amide proton transfer (APT) imaging. Magnetic Resonance in Medicine. 2008;**60**:842-849

[39] Singh A, Cai K, Haris M, Hariharan H, Reddy R. On B_1 Inhomogeneity correction of *in vivo* human brain glutamate chemical exchange saturation transfer contrast at 7T. Magnetic Resonance in Medicine. 2013;**69**:818-824

[40] Windschuh J, Zaiss M, Meissner J-E, Paech D, Radbruch A, Ladd ME, Bachert P. Correction of B_1-inhomogeneities for relaxation-compensated CEST imaging at 7T. NMR in Biomedicine. 2015;**28**:529-537

[41] Schuenke P, Windschuh J, Roeloffs V, Ladd ME, Bachert P, Zaiss M. Simultaneous mapping of water shift and B_1 (WASABI)-application to field-inhomogeneity correction of CEST MRI data. Magnetic Resonance in Medicine. 2017;**77**:571-580

[42] Sun PZ, Farrar CT, Sorensen AG. Correction for artifacts induced by B_0 and B_1 field inhomogeneities in pH-sensitive chemical exchange saturation transfer (CEST) imaging. Magnetic Resonance in Medicine. 2007;**58**:1207-1215

IntechOpen